J. Fluid Mech. (2004), *vol.* 507, *pp.* 309–334.
DOI: 10.1017/S002211200400881X Printed in the United Kingdom

Linear stability analysis of rapid granular flow down a slope and density wave formation

By NAMIKO MITARAI AND HIIZU NAKANISHI

Department of Physics, Kyushu University 33, Fukuoka 812-8581, Japan

(Received 1 April 2003 and in revised form 13 January 2004)

The linear stability of rapid granular flow down a slope under gravity to the longitudinal perturbations is analysed using hydrodynamic equations. It is demonstrated that the steady flow uniform along the flow direction becomes unstable to long-wavelength perturbations longitudinal to the flow direction for certain parameter ranges to form a density wave, in contrast to the finite-wavelength instability for transverse perturbations (Forterre & Pouliquen 2002). It is shown that the instability can be understood as the long-wave instability of kinematic waves in a quasi-one-dimensional system. The results are compared with our previous molecular dynamics simulations (Mitarai & Nakanishi 2001), where spontaneous density wave formation was found.

1. Introduction

Granular flow exhibits a variety of dynamical phenomena, which have been attracting research interest for many years (for reviews, see e.g. Savage 1984 and Jaeger, Nagel & Behringer 1996). Its complex behaviour can be seen even in a simple situation like the gravitational flow on a slope. When the inclination angle is large and the slope is rough, a rapid and relatively low-density flow is realized, and the interaction between grains is dominated by inelastic collisions. On the other hand, when the inclination angle is small, the flow becomes dense and slow, and the frictional interaction plays an important role (Savage 1984; Mitarai & Nakanishi 2003). The comprehensive rheology of the granular flow has not been fully understood yet, except for the rapid collisional flow regime, where hydrodynamic models have been developed with constitutive relations based on the kinetic theory of inelastic hard spheres (Jenkins & Savage 1983; Campbell 1990; Lun *et al.* 1984; Goldhirsh 2003); it has been demonstrated that some quantitative agreement can be achieved for the steady flow by introducing the spinning motion of each grain (Mitarai, Hayakawa & Nakanishi 2002). The steady granular flow, however, turns out to be unstable in various ways, and shows rich phenomena.

In an experiment on a shallow granular flow on a wide slope, Forterre & Pouliquen (2001) have observed that a regular pattern of longitudinal streaks appears along the flow direction. This phenomenon has been analysed by means of the hydrodynamic equations for rapid granular flow (Forterre & Pouliquen 2002). They have calculated the steady solutions and examined their linear stability numerically. They have found that, at a certain parameter region, the steady flow shows the 'inverted density profile', in which the maximum density appears not at the bottom but at a finite distance from the bottom because of the agitation by collisions with the rough solid bottom. It has been shown that the solutions with the 'inverted density profile's are unstable

to perturbations transverse to the flow direction, and the instability results in vortex patterns analogous to the rolls in the Rayleigh–Bérnard convection; the streaks found in the experiment were interpreted as the result of rolls of vortices.

Another instability that has been observed is density wave formation along the flow direction; experimentally, Louge & Keast (2001) have observed jamming patterns travelling upstream in the dense chute flow, and Prasad, Pal & Römkens (2000) have found that waves develop in the shallow flow as they travel downstream. The present authors have performed molecular dynamics simulations of two-dimensional granular flow on a slope and found that the steady flows are unstable to density wave formation when the length of the slope is long enough and/or the particle density is low enough (Mitarai & Nakanishi 2001).

The purpose of this paper is to perform the linear stability analysis on the hydrodynamic equations to investigate the nature of the density wave formation instability found in the experiments and the numerical simulations. The basic method is the same as that used in Forterre & Pouliquen (2002), but we examine the stability to perturbations longitudinal to the flow direction whereas Forterre & Pouliquen (2002) studied transverse stability.

This paper is organized as follows. In § 2, the hydrodynamic model for rapid granular flow is introduced. The steady solutions are numerically obtained in § 3, and the results of the linear stability analysis are presented in § 4. In § 5 a discussion and comparison with the molecular dynamics simulations are given. The results are summarized in § 6.

2. Hydrodynamic equations for granular flows

2.1. *Hydrodynamic equations and constitutive relations*

The hydrodynamic fields for granular flows in three dimensions are the mass density ρ, the mean velocity $\boldsymbol{u}$, and the granular temperature T, where $T = \langle \delta \boldsymbol{u}^2 \rangle / 3$. Here, $\delta \boldsymbol{u} = \boldsymbol{u} - \langle \boldsymbol{u} \rangle$ and $\langle \ldots \rangle$ represents the average over the microscopic scale. Under gravity, they follow

$$\left(\frac{\partial}{\partial t} + \boldsymbol{u} \cdot \nabla \right) \rho = -\rho \nabla \cdot \boldsymbol{u}, \tag{2.1}$$

$$\rho \left(\frac{\partial}{\partial t} + \boldsymbol{u} \cdot \nabla \right) \boldsymbol{u} = \rho \boldsymbol{g} - \nabla \cdot \boldsymbol{\Sigma}, \tag{2.2}$$

$$\frac{3}{2} \rho \left(\frac{\partial}{\partial t} + \boldsymbol{u} \cdot \nabla \right) T = -\nabla \cdot \boldsymbol{q} - \boldsymbol{\Sigma} : \nabla \boldsymbol{u} - \Gamma, \tag{2.3}$$

with the acceleration due to gravity $\boldsymbol{g}$, the stress tensor $\boldsymbol{\Sigma}$, the heat flux $\boldsymbol{q}$, and the energy loss Γ due to the inelastic nature of interactions between grains.

We employ the constitutive relations derived by Lun *et al.* (1984) for a three-dimensional system based on the kinetic theory of inelastic particles:†

$$\boldsymbol{\Sigma} = (p - \zeta \nabla \cdot \boldsymbol{u}) \boldsymbol{I} - 2\mu \boldsymbol{S}, \tag{2.4}$$

$$\boldsymbol{q} = -\kappa \nabla T, \tag{2.5}$$

† The original form of $\boldsymbol{q}$ derived by Lun *et al.* (1984) is $\boldsymbol{q} = -\kappa \nabla T - \kappa_h \nabla \nu$. The coefficient κ_h is proportional to $(1 - e_p)$, thus disappears in the elastic limit. We checked that the influence of the term $\kappa_h \nabla \nu$ on the steady solutions is small in the parameter region considered, therefore neglected this term as did Forterre & Pouliquen (2002).

$$f_1(\nu) = \nu(1 + 4\eta\nu g_0(\nu))$$

$$f_2(\nu) = \frac{5\pi^{1/2}}{96\eta(2-\eta)}\left(1 + \tfrac{8}{5}\eta\nu g_0(\nu)\right)\left(\frac{1}{g_0(\nu)} + \tfrac{8}{5}\eta(3\eta - 2)\nu\right) + \frac{8}{5\pi^{1/2}}\eta\nu^2 g_0(\nu)$$

$$f_3(\nu) = \frac{8}{3\pi^{1/2}}\eta\nu^2 g_0(\nu)$$

$$f_4(\nu) = \frac{25\pi^{1/2}}{16\eta(41 - 33\eta)}\left(1 + \tfrac{12}{5}\eta\nu g_0(\nu)\right)\left(\frac{1}{g_0(\nu)} + \tfrac{12}{5}\eta^2(4\eta - 3)\nu\right) + \frac{4}{\pi^{1/2}}\eta\nu^2 g_0(\nu)$$

$$f_5(\nu) = \frac{12}{\pi^{1/2}}\nu^2 g_0(\nu)$$

$$f_6(\nu) = \frac{\sqrt{3}\pi\nu g_0(\nu)}{2\nu_m f_4(\nu)}$$

$$f_7(\nu) = \frac{\pi\nu g_0(\nu)}{2\sqrt{3}\nu_m f_2(\nu)}$$

TABLE 1. Dimensionless functions used in the constitutive relations and the boundary conditions with $\eta \equiv (1 + e_p)/2$.

where

$$\boldsymbol{S} = \tfrac{1}{2}[\nabla \boldsymbol{u} + (\nabla \boldsymbol{u})^t] - \tfrac{1}{3}(\nabla \cdot \boldsymbol{u})\boldsymbol{I}, \tag{2.6}$$

and

$$\left.\begin{aligned} &p(\nu, T) = \rho_p f_1(\nu) T, \quad \mu(\nu, T) = \rho_p \sigma f_2(\nu) T^{1/2}, \quad \zeta(\nu, T) = \rho_p \sigma f_3(\nu) T^{1/2}, \\ &\kappa(\nu, T) = \rho_p \sigma f_4(\nu) T^{1/2}, \quad \Gamma(\nu, T) = \frac{\rho_p}{\sigma}\left(1 - e_p^2\right) f_5(\nu) T^{3/2}, \end{aligned}\right\} \tag{2.7}$$

with the material density of particle ρ_p, the packing fraction $\nu = \rho/\rho_p$, the particle diameter σ, and the restitution coefficient between particles e_p. Here, $\boldsymbol{I}$ represents the unit matrix. The dimensionless functions $f_i(\nu)$ $(i = 1, \ldots, 5)$ are given in table 1. For the radial distribution function $g_0(\nu)$ in these functions, we adopted the form suggested by Lun & Savage (1986):

$$g_0(\nu) = \frac{1}{(1 - \nu/\nu_m)^{2.5\nu_m}}, \tag{2.8}$$

with the maximum solid fraction ν_m, for which we use 0.60 as in Forterre & Pouliquen (2002).

In the following, all the variables are non-dimensionalized by the length unit σ, the mass unit $\rho_p\sigma^3$, and the time unit $\sqrt{\sigma/g}$. The density field is expressed by the packing fraction ν instead of the mass density ρ. The restitution coefficient between particles is set to be $e_p = 0.7$, the value used in our previous simulations (Mitarai & Nakanishi 2001).

2.2. *Boundary conditions*

The granular flow has a non-zero slip velocity at the solid boundary, where we should impose the momentum and the kinetic energy balances. Sophisticated boundary conditions have been proposed based on microscopic calculations of kinetic theory

for specific geometries (Jenkins & Richman 1986; Richman 1988; Jenkins 1992). We employ, however, a simpler form of the boundary condition obtained from a heuristic approach (Johnson & Jackson 1987; Johnson, Nott & Jackson 1987):

$$-\boldsymbol{n}\cdot\boldsymbol{\Sigma}\cdot\boldsymbol{t} = \eta^*(\nu, T)|\boldsymbol{u}_s|, \tag{2.9}$$

$$\boldsymbol{n}\cdot\boldsymbol{q} = -\boldsymbol{u}_s\cdot\boldsymbol{\Sigma}\cdot\boldsymbol{n} - \Gamma^*(\nu, T), \tag{2.10}$$

where the unit vector $\boldsymbol{n}$ is normal to the floor, $\boldsymbol{u}_s$ is the slip velocity at the floor, and $\boldsymbol{t} = \boldsymbol{u}_s/|\boldsymbol{u}_s|$ is the unit vector in the direction of the slip velocity.

The first equation, (2.9), expresses that the stress at the boundary balances with the momentum transfer due to the collisions between the slope and the flowing grains. The momentum transfer, or right-hand side of (2.9), is assumed to be given by

$$\eta^*(\nu, T)|\boldsymbol{u}_s| = \frac{\pi}{6}\phi|\boldsymbol{u}_s|\Omega(\nu, T), \tag{2.11}$$

with the collision rate $\Omega(\nu, T)$ per unit time per unit area. Here, the factor $\pi/6$ comes from the non-dimensionalization of the particle mass $m = \rho_p\sigma^3\pi/6$. The parameter ϕ characterizes the roughness of the boundary, and the expression means that a fraction ϕ of particle momentum is transferred to the boundary in each collision: therefore, a larger value of ϕ represents a rougher boundary. For the rough boundary in a two-dimensional system with close-packed disks, Jenkins & Richman (1986) estimated $\phi \approx 0.1$, but Forterre & Pouliquen (2002) adopted the smaller value $\phi = 0.05$ for most of the cases because they expected that a boundary with close-packed spheres in a three-dimensional system is smoother on average. In this paper, we mainly use $\phi = 0.05$, but the case of $\phi = 0.10$ is also examined in order to see general trends.

The second equation, (2.10), represents the energy balance, and indicates that the heat flux at the boundary comes from two effects, namely the frictional heating due to the non-zero slip velocity and the energy loss due to inelastic collisions with the floor. The energy loss term Γ^* in (2.10) is given by

$$\Gamma^* = \Phi\frac{\pi}{6}\frac{3}{2}T\Omega(\nu, T) \tag{2.12}$$

with the collision rate $\Omega(\nu, T)$. The parameter Φ represents the rate of energy loss per collision,† and we use $\Phi = 0.39$ in this paper.

For the collision rate $\Omega(\nu, T)$, we use the form adopted by Forterre & Pouliquen (2002), i.e. $\Omega(\nu, T) = \sqrt{3T}\nu g_0(\nu)/\nu_m$: then the expressions for $\eta^*(\nu, T)$ and $\Gamma^*(\nu, T)$ in non-dimensionalized form are

$$\eta^*(\nu, T) = \phi f_7(\nu) f_2(\nu) T^{1/2}, \tag{2.13}$$

$$\Gamma^*(\nu, T) = \tfrac{1}{2}\Phi f_6(\nu) f_4(\nu) T^{3/2}, \tag{2.14}$$

where the dimensionless functions $f_6(\nu)$ and $f_7(\nu)$ are given in table 1.

At infinity, we impose the condition that the stress and the heat flux vanish, namely

$$\boldsymbol{\Sigma} \to 0 \quad \text{and} \quad \boldsymbol{q} \to 0 \quad \text{as} \quad y \to \infty, \tag{2.15}$$

where the y-axis is taken perpendicular to the floor (figure 1).

† Johnson & Jackson (1987) explicitly relate Φ to the restitution coefficient between the floor and the particles e_w in the form $\Phi = (1 - e_w^2)$, but we adopt (2.12) as a more general expression.

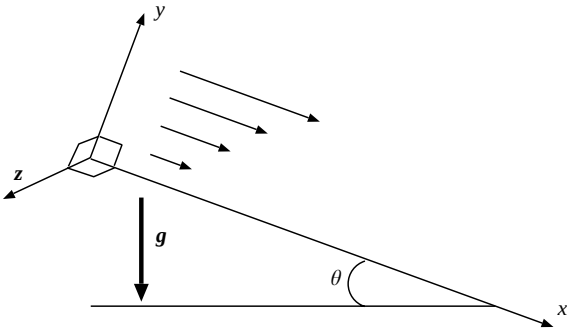

FIGURE 1. The coordinate system.

3. Steady flows

3.1. *Equations and numerical method*

First, we consider the steady solution which is uniform along the slope for (2.1)–(2.3) with the boundary conditions (2.9), (2.10), and (2.15) in the form

$$\nu(x, y, z, t) = \nu_0(y), \tag{3.1}$$

$$\boldsymbol{u}(x, y, z, t) = (u_0(y), 0, 0), \tag{3.2}$$

$$T(x, y, z, t) = T_0(y), \tag{3.3}$$

where we take the x-axis along the slope, the y-axis perpendicular to the floor, and the z-axis perpendicular to the (x, y)-plane (figure 1).

Then, equations (2.1)–(2.3) are written as

$$0 = \nu_0 \sin\theta - \frac{\mathrm{d}\Sigma^0_{xy}}{\mathrm{d}y}, \tag{3.4}$$

$$0 = -\nu_0 \cos\theta - \frac{\mathrm{d}\Sigma^0_{yy}}{\mathrm{d}y}, \tag{3.5}$$

$$0 = -\Sigma^0_{xy}\frac{\mathrm{d}u_0}{\mathrm{d}y} - \frac{\mathrm{d}q^0_y}{\mathrm{d}y} - \Gamma^0, \tag{3.6}$$

where the superscript 0 denotes that the functions are for the steady solution, namely $\boldsymbol{q}^0 = -\kappa(\nu_0, T_0)\nabla T_0 = (0, q^0_y, 0)$, etc. By integrating (3.4) and (3.5) over y with the stress-free condition at infinity, we obtain the condition

$$\Sigma^0_{xy} = -\tan\theta\ \Sigma^0_{yy}. \tag{3.7}$$

From (3.4)–(3.7) and the constitutive relations, we have

$$\nu_0'(y) = -\frac{f_1^0 T_0' + \nu_0 \cos\theta}{f^0_{1,\nu} T_0}, \tag{3.8}$$

$$u_0'(y) = \frac{f_1^0 T_0^{1/2}}{f_2^0}\tan\theta, \tag{3.9}$$

$$T_0''(y) = \frac{1}{f_4^0}\left[\left(1 - e_p^2\right) f_5^0 T_0 - f_2^0 u_0' - f^0_{4,\nu}\nu_0' T_0' - \frac{(T_0')^2}{2T_0} f_4^0\right], \tag{3.10}$$

where $f_i^0 \equiv f_i(\nu_0)$, $f^0_{i,\nu} \equiv (\mathrm{d}/\mathrm{d}\nu) f_i(\nu)|_{\nu=\nu_0}$, and the prime indicates the derivative by its argument.

The boundary conditions (2.9) and (2.10) at the floor ($y = 0$) for the steady solution can be written as

$$T_0 = \left(\frac{\phi f_2^0 f_7^0}{f_1^0 \tan\theta} u_0 \right)^2, \tag{3.11}$$

$$T_0' = -f_6^0 \left(\tfrac{1}{3}\phi u_0^2 - \tfrac{1}{2}\Phi T_0 \right). \tag{3.12}$$

The boundary condition (2.15) that the stress and the energy flux should vanish at infinity is satisfied when (Ahn, Brennen & Sabersky 1992)

$$T_0'(y) \to 0 \quad \text{as} \quad y \to \infty. \tag{3.13}$$

In order to obtain the steady solutions, we integrate (3.8), (3.9), and (3.10) numerically using the fourth-order Runge–Kutta method with the boundary conditions (3.11) and (3.12). We employ the shooting method to find the solution which satisfies the condition (3.13) (Forterre & Pouliquen 2002): for a given inclination angle θ and a given density at the floor $\nu_0(0)$, we search for a solution by adjusting the value of the velocity at the floor $u_0(0)$. In the actual calculations, we integrate the equations numerically from $y = 0$ to a certain height $y_{\max}$, and search for the solution which gives $|T_0'(y_{\max})| < 10^{-7}$. The value of $y_{\max}$ is chosen to be large enough in comparison with the relaxation length, which depends on the parameters and can be determined only after the solution is obtained.

We use θ and $\nu_0(0)$ to specify the solution in the rest of the paper.

3.2. *Numerical solutions*

For a given roughness ϕ of the slope, steady solutions are found for a certain range of the slope inclination angle θ (Forterre & Pouliquen 2002). We present the steady solutions for two cases, (i) $\phi = 0.05$ and (ii) $\phi = 0.10$; most of the results are for $\phi = 0.05$, and the case of $\phi = 0.10$ will be given to examine general trend.

3.2.1. *The case of* $\phi = 0.05$

For an appropriate θ, there exist steady solutions for a given density at the floor $\nu_0(0)$. We numerically find the steady solution for the range $8^\circ \lesssim \theta \lesssim 20^\circ$ for moderate density; towards the lower limit of θ, the length scale of the density decay in the y-direction tends to zero and becomes smaller than the particle diameter, which is physically unacceptable, while the decay length of the density diverges towards the upper limit of θ. This is consistent with the analysis by Anderson & Jackson (1992) that the steady solution in the high-density limit is allowed for a finite range of θ.†

For a given steady solution, we define the 'thickness' h and the 'mean density' $\bar{\nu}$: the thickness h is the value of y where the density is 1% of the maximum density, and the mean density $\bar{\nu}$ is given by

$$\bar{\nu} = \frac{1}{h} \int_0^\infty \nu_0(y)\, \mathrm{d}y. \tag{3.14}$$

It has been found numerically by Forterre & Pouliquen (2002) that a one to one correspondence exists between $(\theta, \nu_0(0))$ and $(h, \bar{\nu})$.

Figure 2(*a*) shows the contour lines of θ in the $(h, \bar{\nu})$-plane, where θ increases from left to right. In this plot, it is clear that h goes to zero as θ decreases and h diverges

† Anderson & Jackson (1992) distinguished two cases of steady solutions, and our parameter values are found to be in their "Case 1".

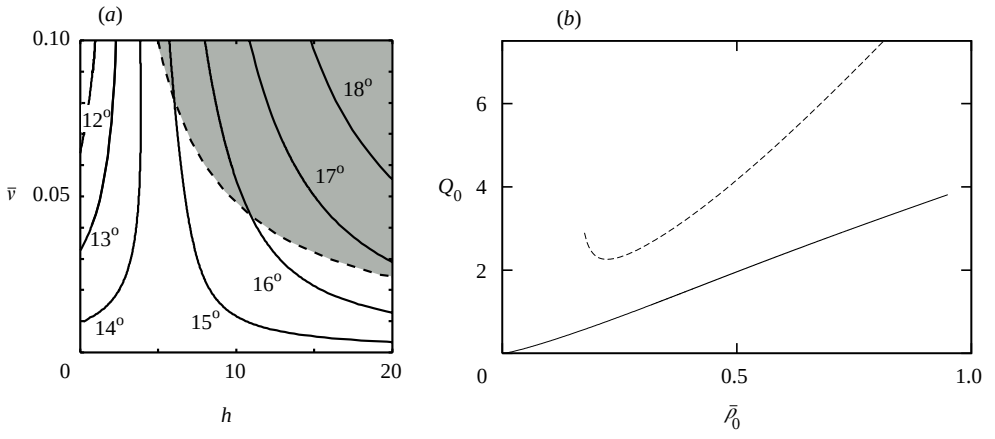

FIGURE 2. (*a*) The contour lines of θ in the $(h, \bar{\nu})$-plane for $\phi = 0.05$. The region of non-monotonic density profiles is shown in grey. (*b*) The flux Q_0 vs. the one-dimensional density $\bar{\rho}_0$ for $\phi = 0.05$. The solid line and the dashed line are for $\theta = 14^\circ$ and $\theta = 16^\circ$, respectively.

as θ increases. There is a separatrix near the bottom at $h \approx 7$, where the value of θ is around 15°; the contour line for $\theta \leqslant 14^\circ$ tends to $h = 0$ as $\bar{\nu}$ decreases, while h diverges along the contour lines for $\theta \geqslant 15^\circ$ as $\bar{\nu}$ becomes small.

The difference between $\theta \geqslant 15^\circ$ and $\theta \leqslant 14^\circ$ can be seen in the relation between the flux Q_0 and the one-dimensional density $\bar{\rho}_0$ defined as

$$Q_0 \equiv \int_0^\infty \nu_0(y) u_0(y)\, \mathrm{d}y \quad \text{and} \quad \bar{\rho}_0 \equiv \int_0^\infty \nu_0(y)\, \mathrm{d}y, \tag{3.15}$$

respectively, for a fixed inclination angle. It is found that Q_0 is an increasing function of $\bar{\rho}_0$ for $\theta \leqslant 14^\circ$, while Q_0 has a minimum at a finite $\bar{\rho}_0$ for $\theta \geqslant 15^\circ$; the plot of Q_0 vs. ρ_0 is shown in figure 2(*b*) for $\theta = 14^\circ$ and $\theta = 16^\circ$.

Typical profiles of the density, the velocity, and the temperature for $\theta = 16^\circ$ are shown in figure 3 for the density at the floor $\nu_0(0) = 0.04$–0.15. We see in figure 3(*a*) that the density decays monotonically when the density at the floor $\nu_0(0)$ is small enough ($\nu_0(0) \leqslant 0.10$), while for higher density ($\nu_0(0) = 0.15$) the maximum density appears at a finite height. The region where the maximum density appears at a finite height is shown in figure 2(*a*) as a grey region. We focus on the lower density region because the density was found to decay monotonically in our previous simulation (Mitarai & Nakanishi 2001; Mitarai *et al.* 2002).

For $\nu_0(0) \lesssim 0.10$, the higher density flow shows lower flow speed in the case of $\theta = 16^\circ$, which results in the decrease of the flux Q_0 as $\bar{\rho}_0$ increases for $\bar{\rho}_0 \lesssim 0.2$ (figure 2*b*). For higher density ($\nu_0(0) = 0.15$ in figure 3), the flow speed increases with $\bar{\rho}_0$, which causes the increase of the flux Q_0 for higher $\bar{\rho}_0$. As a result, Q_0 has a minimum at a finite density.

In the case of $\theta \leqslant 14^\circ$, the velocity continuously decreases as the density becomes lower, and Q_0 becomes an increasing function of $\bar{\rho}_0$.

3.2.2. *The case of* $\phi = 0.10$

The slope is rougher than the previous case, and the steady solution exists for $12^\circ \lesssim \theta \lesssim 25^\circ$. The contour lines for θ in the $(h, \bar{\nu})$-plane are shown in figure 4(*a*). As in the case of $\phi = 0.05$, h goes to zero as the density becomes lower for smaller

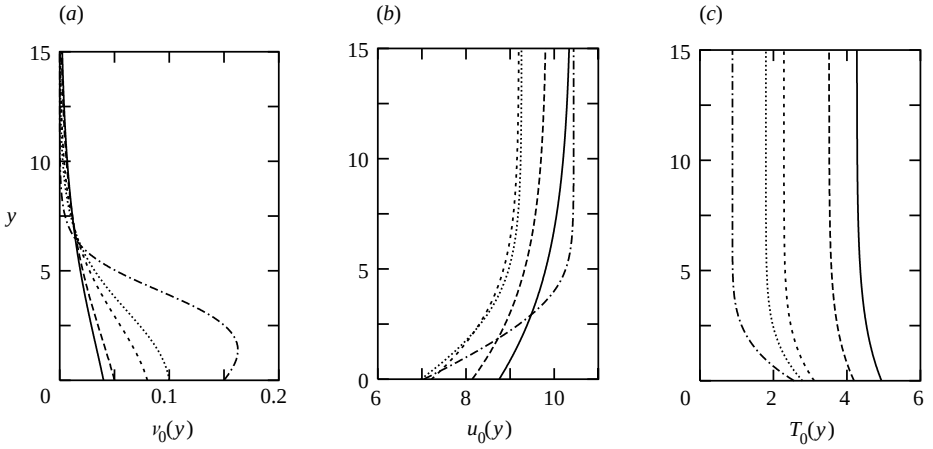

FIGURE 3. The steady solutions for $\phi = 0.05$ and $\theta = 16°$: (*a*) density profiles; (*b*) velocity profiles; (*c*) temperature profiles. Different line types correspond to solutions with different densities: $\nu_0(0) = 0.04$ (solid lines), 0.05 (long-dashed lines), 0.08 (short-dashed lines), 0.10 (dotted lines), and 0.15 (dash-dotted lines).

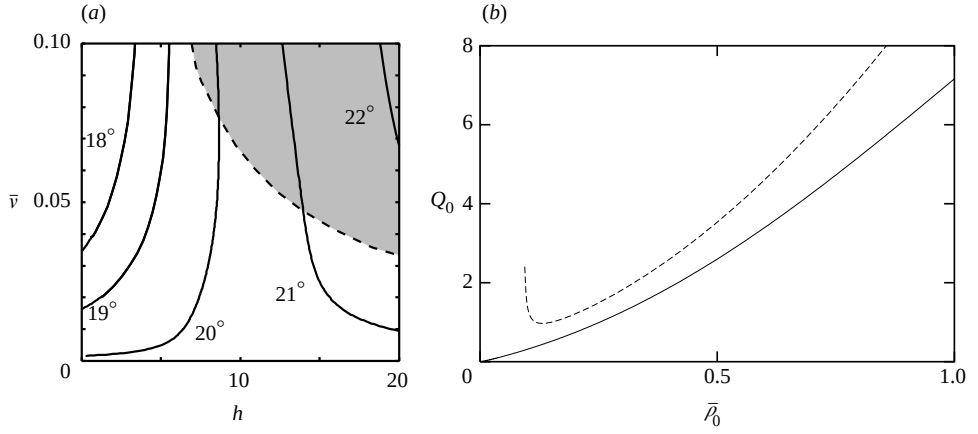

FIGURE 4. (*a*) The contour lines of θ in the $(h, \bar{\nu})$-plane for $\phi = 0.10$. The region of non-monotonic density profiles is shown in grey. (*b*) Q_0 vs $\bar{\rho}_0$ for $\phi = 0.10$. The solid line and the dashed line are for $\theta = 20°$ and $\theta = 21°$, respectively.

θ, while h diverges for smaller density when θ is large enough. Figure 4(*b*) shows the $\bar{\rho}_0$ dependence of Q_0, which is a monotonically increasing function for $\theta = 20°$ and has a minimum for $\theta = 21°$. The typical solutions are shown for $\theta = 20°$ in figure 5. For large enough h and $\bar{\nu}$, the maximum density appears at a finite distance from the floor. The region of the non-monotonic density profile is shown by a grey region in figure 4(*a*).

4. Linear stability analysis; density wave formation

4.1. *Normal mode analysis*

We restrict our stability analysis to a perturbation uniform along the z-direction, because we are interested in the instability along the flow direction. The flow is

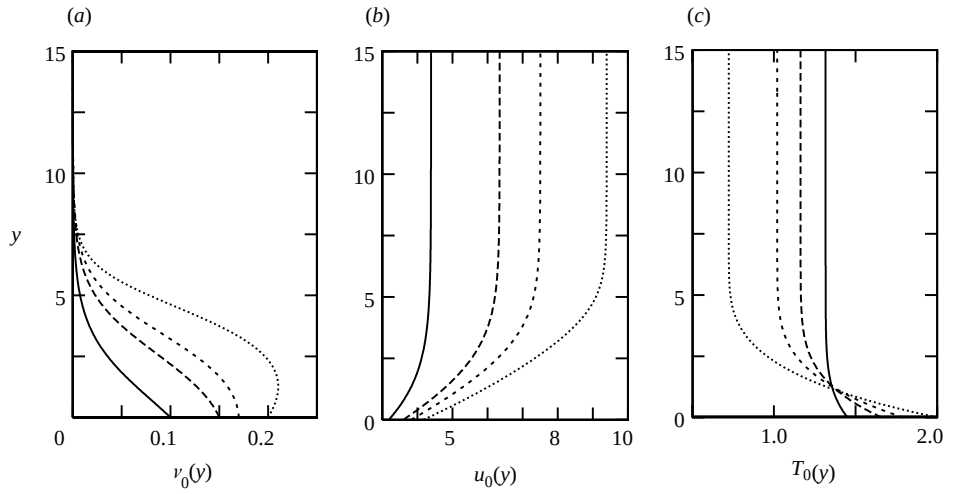

FIGURE 5. The steady solutions for $\phi = 0.10$ and $\theta = 20°$: (*a*) density profiles; (*b*) velocity profiles; (*c*) temperature profiles. Different line types correspond to solutions with different densities: $\nu_0(0) = 0.10$ (solid lines), 0.15 (long-dashed lines) 0.17 (short-dashed lines), and 0.20 (dotted lines).

perturbed around the steady solution as

$$\nu(x, y, t) = \nu_0(y) + \nu_1(x, y, t), \tag{4.1}$$

$$\boldsymbol{u}(x, y, t) = (u_0(y), 0, 0) + (u_1(x, y, t), v_1(x, y, t), 0), \tag{4.2}$$

$$T(x, y, t) = T_0(y) + T_1(x, y, t). \tag{4.3}$$

The governing equations and the boundary conditions are linearized with respect to the deviations ν_1, u_1, v_1, and T_1; the resulting expressions are rather lengthy and given in Appendix A.

Now we look for the normal modes for the density, the velocity, and the temperature perturbations of the form

$$(\nu_1, u_1, v_1, T_1) = \mathrm{Re}[(\hat{\nu}(y), \hat{u}(y), \hat{v}(y), \hat{T}(y)) \exp(\alpha t + \mathrm{i}kx)]. \tag{4.4}$$

The flow is linearly unstable if $\mathrm{Re}(\alpha) > 0$.

As for the boundary condition at the free surface, the asymptotic behaviour of the perturbations at large y is used. When y is much larger than the decay length of the density and thus $\nu_0(y)$ is very small, the density perturbation should also decay ($\hat{\nu} \propto \nu_0$), and $\hat{u}$, $\hat{v}$, and $\hat{T}$ decay proportionally to $\exp(-ky)$ (Forterre & Pouliquen 2002); therefore, we imposed the boundary condition that

$$\hat{u}'(y) = -k\hat{u}(y), \quad \hat{v}'(y) = -k\hat{v}(y), \quad \hat{T}'(y) = -k\hat{T}(y), \tag{4.5}$$

at $y = y_{\max}$; $y_{\max}$ is a large enough height such that $\nu_0(y_{\max}) < 10^{-9}$, in addition to the condition $|T_0'(y_{\max})| < 10^{-7}$ discussed in § 3.

We solve the eigenvalue problems of the linearized equations (A 1)–(A 4) for (4.4) numerically using the Chebychev collocation method with the discretization in the y-direction (Gottlieb, Hussaini & Orszag 1984; Canuto *et al.* 1988; Boyd 2001; Forterre & Pouliquen 2002). It is known that the straightforward discretization of space requires two extra boundary conditions (Malik 1990; Forterre & Pouliquen 2002), for which we use the momentum balance condition in the y-direction at $y = 0$ and the decay condition for the density perturbation, i.e. $\hat{v}'(y) = -(\cos\theta / T_0(y))\hat{v}(y)$ at

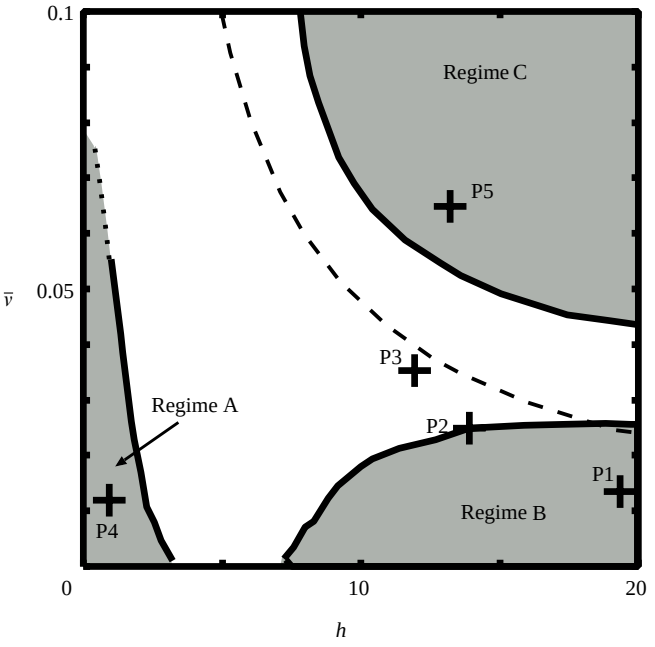

FIGURE 6. The stability diagram for h vs. $\bar{\nu}$ for $\phi = 0.05$, where the unstable (stable) regimes are shown in grey (white). We find three unstable regimes A, B, and C. The dashed line shows the boundary between the region of non-monotonic density profiles and that of the monotonic density profiles (see also figure 2). The dispersion relations at the points P1–P5 are shown in figures 7–9. The region of $h < 1$ where the stability boundary is shown by a dotted line was not examined in detail because a flow with decay length less than the particle diameter is physically unacceptable.

$y = y_{\max}$. In the numerics, to solve the generalized eigenvalue problem in the form $A\boldsymbol{V} = \alpha B\boldsymbol{V}$ for the complex eigenvalues α and the eigenvectors $\boldsymbol{V}$, we used LAPACK version 3.0 (Anderson *et al.* 1999). The discretization number N_d is about 100.

The numerically obtained eigenmodes contain unphysical modes, called spurious modes, due to the discretization (Mayer & Powell 1992; Boyd 2001; Forterre & Pouliquen 2002). For the spurious modes, it is known that the Chebychev coefficients of higher wavenumber are large, and the eigenvalues are sensitive to small change of N_d. We determine that the eigenmodes are physical ones by checking that their Chebychev coefficients for higher wavenumber are small and their eigenvalues vary little upon changing N_d. We confirmed that, for these modes, the highest ten coefficients are less than 10^{-7} when the eigenvectors are normalized so that the sum of the absolute values of the real part and the imaginary part of the largest component becomes one, and the variation of the eigenvalues through small change of N_d are less than 10^{-7}.

4.2. *Stability diagram, dispersion relations, and eigenfunctions*

We present the results of the linear stability analysis in the cases of $\phi = 0.05$ and $\phi = 0.10$, for which the steady solutions are shown in § 3.2.

4.2.1. *The case of* $\phi = 0.05$

The stability diagram is shown in figure 6 in the parameter space of h vs. $\bar{\nu}$. The unstable (stable) regimes are shown by grey (white) regions, and the boundary

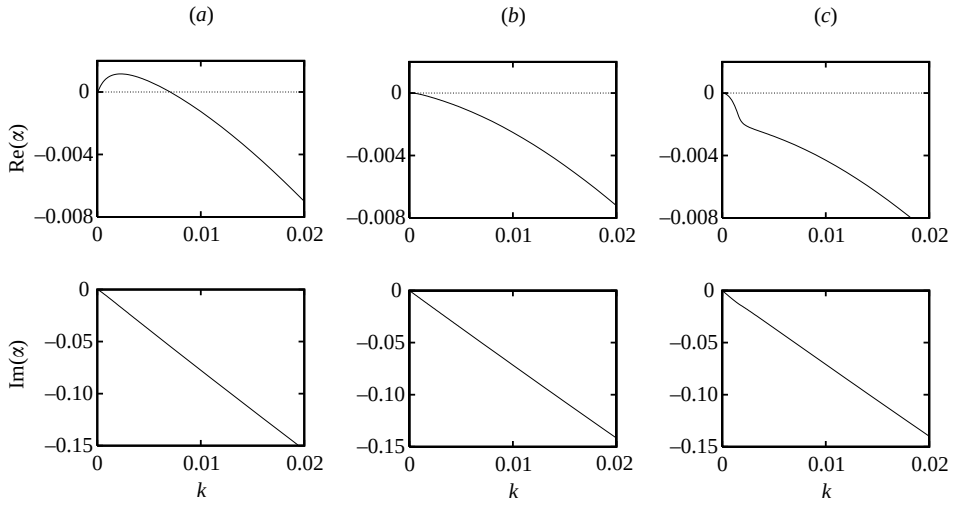

FIGURE 7. The dispersion relations of the least stable mode for the steady solutions with $\phi = 0.05$ and $\theta = 16^\circ$ for (*a*) $\nu_0(0) = 0.05$, (*b*) 0.08, and (*c*) 0.10, which correspond to the points P1, P2, and P3 in figure 6, respectively.

between the regions of monotonic and non-monotonic density profiles is shown by a dashed line. Within the investigated region, we find three unstable regimes: regime A at small h and small $\bar{\nu}$; regime B at large h and small $\bar{\nu}$; and the regime C at large h and large $\bar{\nu}$. When we decrease the density with a constant inclination angle (along a contour in figure 2), we will eventually encounter either regime A or regime B, namely a flow with low enough density is always unstable. The two regimes have different steady flow behaviour as we have seen already: in regime A on the small-h side, the flow becomes slower as the density becomes smaller, while in regime B on the large-h side the flow is faster for the smaller density. On the other hand, the denser flow can be unstable in regime C, which lies within the region of non-monotonic density profiles. In this regime, the denser flow is faster as in regime A.

The dispersion relations of the least stable modes $\alpha = \alpha(k)$ are shown in figure 7 for $\theta = 16^\circ$ and $\nu_0(0) = 0.05$ (*a*), 0.08 (*b*), and 0.10 (*c*), which correspond to the points P1, P2, and P3, respectively, in the stability diagram of figure 6; P1 lies within the unstable regime B. In all cases, it is found that the least stable mode satisfies $\alpha(0) = 0$. The growth rate $\mathrm{Re}(\alpha)$ is positive for $\nu_0(0) = 0.05$ for $0 < k \leqslant k_c$ with $k_c \approx 0.007$ (figure 7*a*). The magnification around $k = 0$ in figure 8 shows that $\mathrm{Re}(\alpha)$ grows quadratically in k for small k. As $\nu_0(0)$ is increased, the maximum value of $\mathrm{Re}(\alpha)$ decreases and becomes negative for all k (figure 7*b*, *c*).

The dispersion relations for the unstable modes at P4 (in regime A) and at P5 (in regime C) are shown in figure 9 for $(\theta, \nu_0(0)) = (14^\circ, 0.05)$ (*a*) and $(17^\circ, 0.10)$ (*b*), respectively. The instability occurs for the long-wavelength perturbation, and both of the dispersion relations show that $\alpha(0) = 0$ and a growth rate quadratic in k for small k, i.e. $\mathrm{Re}(\alpha(k)) \propto k^2$; these features are the same as those in the unstable regime B.

The least stable eigenmodes for $\theta = 16^\circ$ at $k = 0.002$ are shown for two cases: the stable case of $\nu_0(0) = 0.10$ (P3 in figure 6) in figure 10 and the unstable case of $\nu_0(0) = 0.05$ in the regime B (P1 in figure 6) in figure 11, over one wavelength $\lambda = 2\pi/k$. The contours in figures 10(*a*) and 11(*a*) show the density eigenfunctions; the lighter (darker) regions indicate positive (negative) regions, and the arrows represent

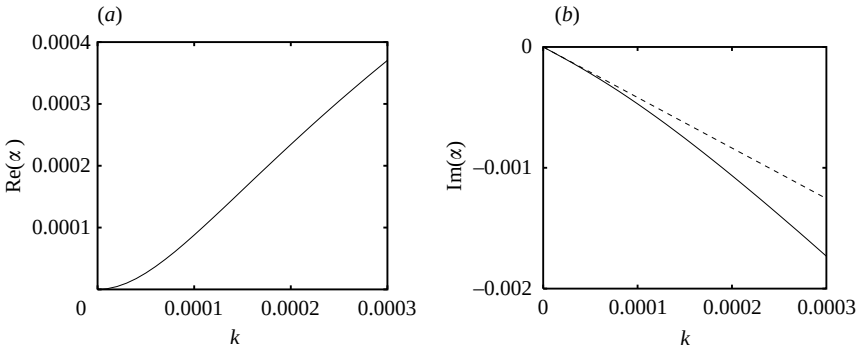

FIGURE 8. A magnification of the dispersion relations near $k = 0$ of the unstable stable mode for the steady solutions with $\phi = 0.05$ and $\theta = 16^\circ$ for $\nu_0(0) = 0.05$ at P1 in the regime B. $\mathrm{Re}(\alpha)$ grows quadratically in k, while the slope of $\mathrm{Im}(\alpha)$ is given by $-\mathrm{d}Q_0/\mathrm{d}\bar{\rho}_0$ in the long-wavelength limit, which is shown by a dashed line.

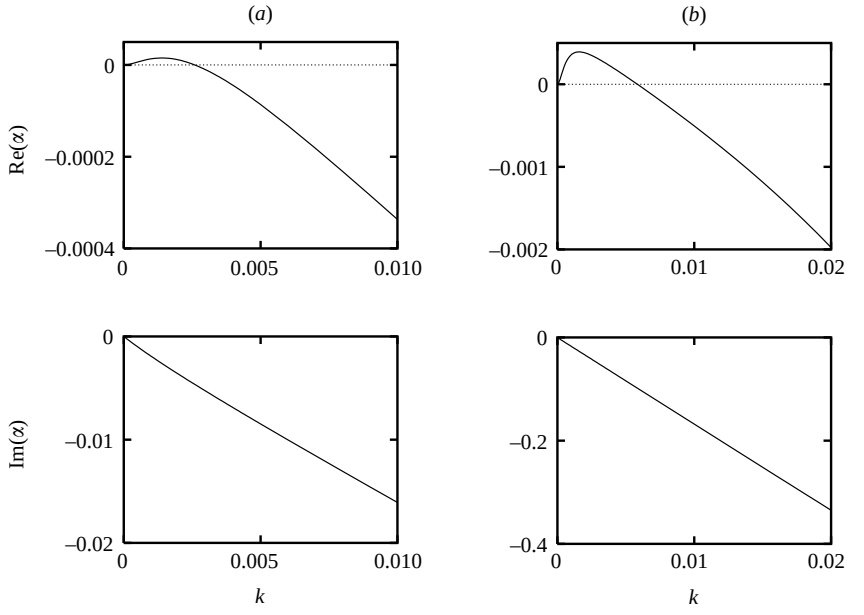

FIGURE 9. The dispersion relations of the unstable mode for $\phi = 0.05$ with (*a*) $\theta = 14^\circ$ and $\nu_0(0) = 0.05$ (P4; in regime A) and (*b*) $\theta = 17^\circ$ and $\nu_0(0) = 0.10$ (P5; in regime C).

the corresponding velocity eigenfunctions. In both figures near $y = 0$, we see that the velocity perturbations point in the positive (negative) x-direction in regions of negative (positive) density perturbation. The contours for the corresponding temperature eigenfunctions plotted in figures 10(*b*) and 11(*b*) show that the regions where the density perturbation is negative (darker regions in figures 10*a* and 11*a*) roughly correspond to positive temperature perturbations (lighter regions in figures 10*b* and 11*b*).

The difference between the stable mode (figure 10) and the unstable mode (figure 11) is seen if we focus on the divergence of the velocity perturbation. In the case of the stable mode for $\nu_0(0) = 0.10$ (figure 10*a*), the grains flow into the region where the density perturbation is negative (see the region around $x \approx \lambda/2$ and $y \approx 2$), thus

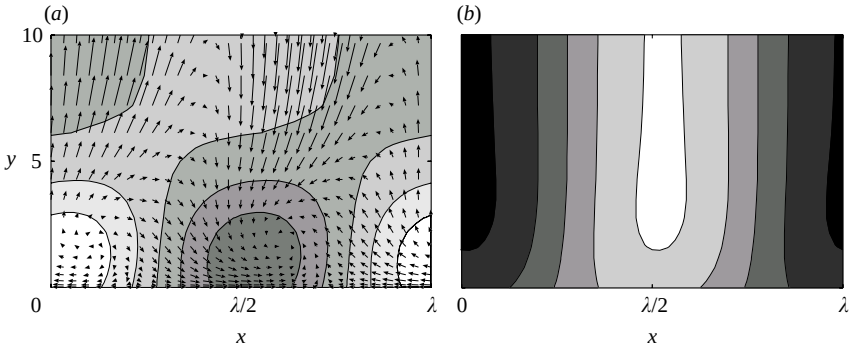

FIGURE 10. The eigenfunctions of the least stable mode for $\phi = 0.05$, $\theta = 16°$, and $\nu_0(0) = 0.10$ (P3 in figure 6), whose wavenumber is $k = 0.002$. λ is the wavelength of this eigenmode, $\lambda = 2\pi/k$. Contours of (*a*) the density and (*b*) the temperature eigenfunctions are shown by grey scale, where the lighter (darker) region corresponds to the larger positive (negative) value. The arrows in (*a*) indicate the corresponding velocity eigenfunction. They shows that the grains flow from the lighter region into the darker density region, namely the density perturbation decays. Note that the temperature perturbation is negative in the region of positive density perturbation.

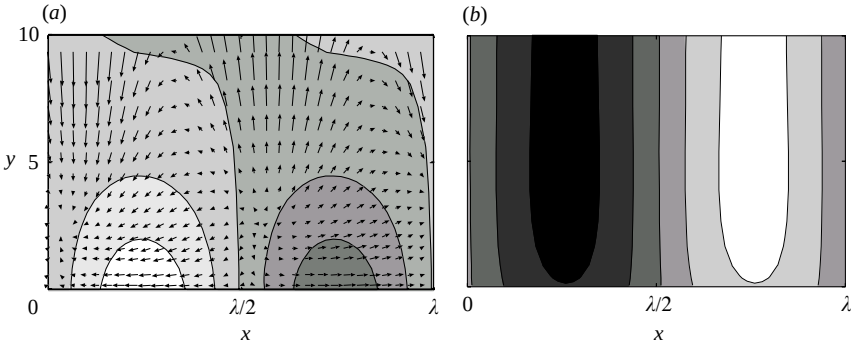

FIGURE 11. The eigenfunctions of the unstable mode for $\phi = 0.05$, $\theta = 16°$, and $\nu_0(0) = 0.05$ (P1 in figure 6), whose wavenumber is $k = 0.002$. Contours of the density eigenfunction and the velocity eigenfunction in (*a*) show that the grains flow from the region of negative density perturbation into that of positive perturbation, namely the perturbation is amplified and results in the formation of density wave. The temperature perturbation in (*b*) is negative in the region of positive density perturbation.

the density perturbation has negative feedback. On the other hand, in the case of the unstable mode for $\nu_0(0) = 0.05$ (figure 11*a*), the grains flow into the region where the density perturbation is positive (see the region around $x \approx 0$ and $y \approx 3$). As a result, the perturbation grows and eventually causes the nonlinear density wave.

The eigenfunctions of the unstable modes at P4 in regime A and at P5 in regime C show some different characteristics from those at P1 in the regime B. Reflecting the difference in the steady flow between regimes A and C and regime B, the denser parts of the density eigenfunctions roughly correspond to the region where the velocity fluctuation has positive component in the direction parallel to the mean flow. For all three regimes, however, the unstable modes show that the grains flow into the region of positive density perturbation; this suggests that the instability leads to the density wave in regimes A and C as in regime B.

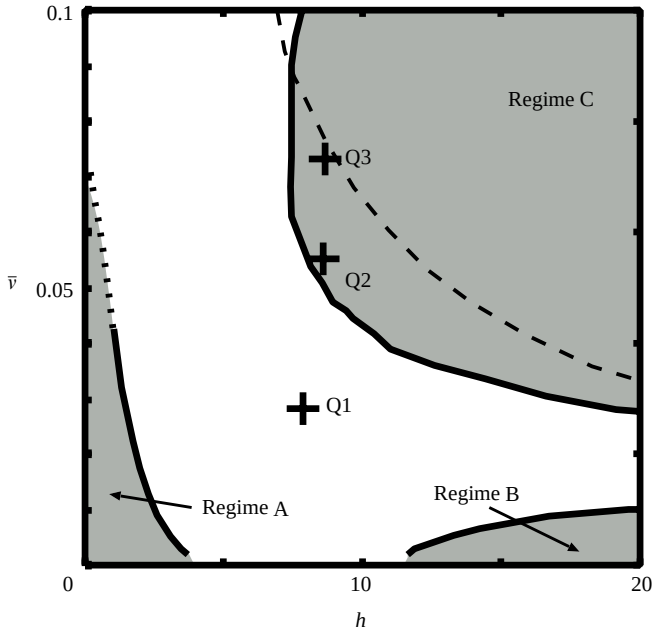

FIGURE 12. The stability diagram for h vs. $\bar{\nu}$ with $\phi = 0.10$, where the unstable (stable) regimes are shown in grey (white). We find three unstable regimes A, B, and C. The dashed line shows the boundary between the region of non-monotonic density profiles and that of monotonic density profiles (see also figure 4). The dispersion relations at the points Q1–Q3 are shown in figure 13.

4.2.2. *The case of* $\phi = 0.10$

The stability diagram for $\phi = 0.10$ is shown in figure 12. As in the case of $\phi = 0.05$, there are three unstable regimes, but the qualitative difference is that the unstable regime C for large h and large $\bar{\nu}$ contains part of the region of monotonic density profiles as well as that of non-monotonic density profiles. The dispersion relations around the boundary of regime C are shown in figure 13 for $\theta = 20^\circ$ and $\nu_0(0) = 0.10$ (a), 0.15 (b) and 0.17 (c), which correspond to the points Q1, Q2, and Q3, respectively, in the stability diagram 12. It is seen that the instability occurs to the long-wavelength perturbation.

The unstable eigenmodes for $\theta = 20^\circ$ and $\nu_0(0) = 0.17$ (Q3 in figure 12) with $k = 0.002$ are shown in figure 14. The density and velocity eigenfunctions indicate that the grains flow into the region of positive density perturbation (see the region around $x \approx \lambda/2$, $y \approx 0$; a magnification is shown (c)); thus the density perturbation will grow. The difference from the case in figure 11 is that the velocity perturbation at the floor ($y = 0$) is in the positive x-direction in the region of positive density perturbation; namely, the particles flow faster in the region where they become dense.

5. Discussion

We have calculated the steady flow solutions and examined their linear stability under a longitudinal perturbation in the cases of $\phi = 0.05$ and $\phi = 0.10$. The linear stability analysis revealed that there are three unstable regimes, A, B, and C, in the $(h, \bar{\nu})$-plane in both cases. Regimes A and B are in the small-$\bar{\nu}$ region, while regime

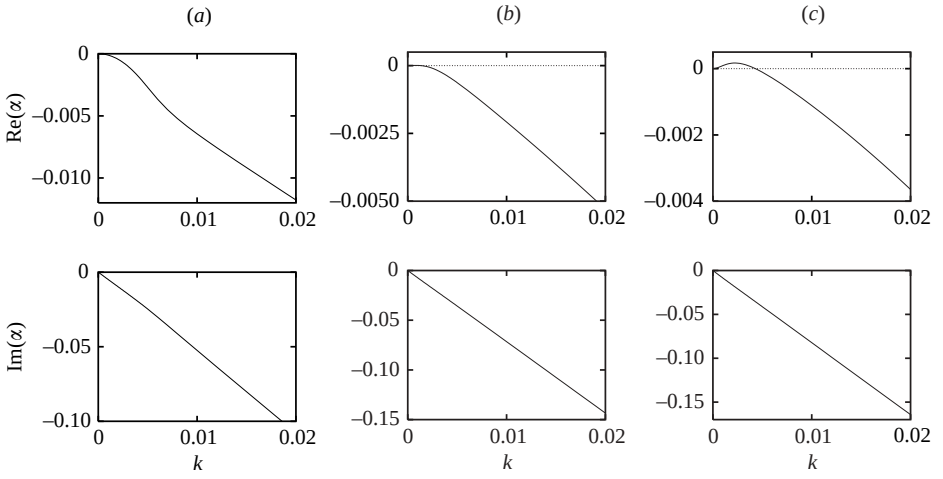

FIGURE 13. The dispersion relations of the least stable mode with $\phi = 0.10$ and $\theta = 20^\circ$ for $\nu_0(0) = 0.10$ (*a*); 0.15 (*b*); 0.17 (*c*), which correspond to the points Q1, Q2, and Q3 in figure 12, respectively.

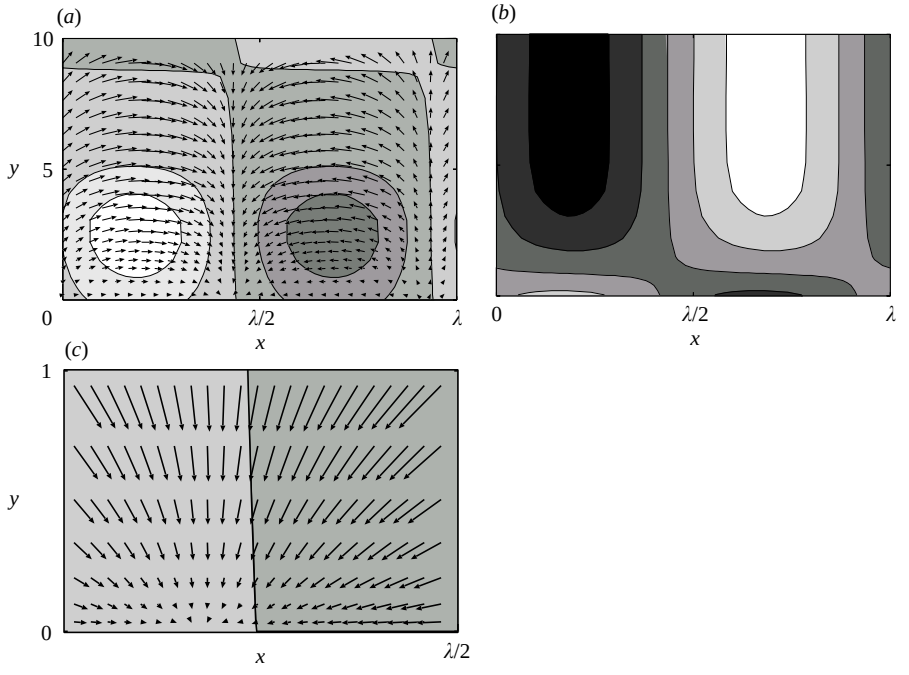

FIGURE 14. The eigenfunctions of the unstable mode for $\phi = 0.10$, $\theta = 20^\circ$, and $\nu_0(0) = 0.17$ (Q3 in figure 12), whose wavenumber is $k = 0.002$. Contours of the density eigenfunction and the velocity eigenfunction in (*a*) show that the grains flow into the region of the positive density perturbation. In (*b*), contours of the temperature perturbation are shown. (*c*) A magnification of (*a*) around $x \approx \lambda/2$, $y \approx 1$.

C is in the large-$\bar{\nu}$ region. The difference between regimes A and B is the density dependence of the flow velocity: the denser flow is faster in regime A, while the flow with lower density is faster in regime B. Regime C lies within the region where the density profile is non-monotonic in the case of $\phi = 0.05$, but includes part of the

region of monotonic density profiles for $\phi = 0.10$, although the region of regime C roughly corresponds with that of non-monotonic density profiles. In all the regimes, the dispersion relation of the unstable mode shows the features that (i) $\alpha(0) = 0$ and (ii) $\mathrm{Re}(\alpha(k)) \propto k^2$ for small k. The unstable eigenmodes obtained suggest that the instability causes a density wave.

In this section, we discuss the mechanism of the instability, a compare with simulations, and the relationship with the transverse instability studied by Forterre & Pouliquen (2002).

5.1. *Mechanism of the instability*

5.1.1. *Kinematic wave and the long-wave instability*

The long-wavelength instability which results in a density wave is well-known for quasi-one-dimensional flows, such as wave formation in film flow (Smith 1993; Ooshida 1999), density wave formation in the granular flow in a narrow vertical pipe (Raafat, Hulin & Herrmann 1996; Moriyama *et al.* 1998), and formation of jams in traffic flow (Kerner & Konhäuser 1993; Bando *et al.* 1995; Mitarai & Nakanishi 2000*a*, *b*). This instability is closely related to the continuity of 'density' $\bar{\rho}$ (the thickness in the case of incompressible fluid, the density per unit length along the pipe for granular flow, or the density of cars for traffic flow): $\bar{\rho}$ obeys the equation of continuity in the form

$$\frac{\partial \bar{\rho}(x,t)}{\partial t} + \frac{\partial Q(x,t)}{\partial x} = 0, \tag{5.1}$$

where Q is the flux. The flux Q may be expressed in terms of $\bar{\rho}$ and its spatial derivatives, but may also depend on time especially when the inertia effect exists. In the long-wavelength and the long-time limit, the effect of the spatial derivatives of $\bar{\rho}$ and inertia on Q may be neglected. Then the flux is determined by the density, $Q(x,t) = Q_0(\bar{\rho}(x,t))$, and equation (5.1) becomes

$$\frac{\partial \bar{\rho}(x,t)}{\partial t} - c\frac{\partial \bar{\rho}(x,t)}{\partial x} = 0 \quad \text{with} \quad c = -\frac{\mathrm{d}Q_0(\bar{\rho})}{\mathrm{d}\bar{\rho}}. \tag{5.2}$$

The wave that can be described by this equation is called the kinematic wave (Whitham 1974). The effect of inertia and spatial derivatives for small but non-zero wavelength appears as the growth rate quadratic in k (Whitham 1974; Ooshida 1999), which causes the instability to yield a density wave. The actual form of the flux Q depends on the physical system, but we call the instability caused through this mechanism 'the long-wave instability' after Smith (1993). Note that the unstable mode caused by the long-wave instability has the following three features for the complex growth rate $\alpha(k)$: (i) $\alpha(0) = 0$, (ii) $\mathrm{Re}(\alpha(k)) \propto k^2$ for small k, and (iii) the phase velocity of the least stable mode $c = \mathrm{Im}(\alpha(k))/k$ is given by $-\mathrm{d}Q_0/\mathrm{d}\bar{\rho}$ in the long-wavelength limit.

The unstable modes obtained in the present analysis of the two-dimensional flow down a slope satisfy all of the features (i), (ii) and (iii); (i) and (ii) have been already pointed out in the text, and (iii) can be seen in figure 8(*b*) for $\phi = 0.05$, $\nu_0(0) = 0.05$, and $\theta = 16^\circ$. In fact, (iii) can be demonstrated using (i) and the equation of continuity (2.1) as shown in Appendix B.

These features strongly suggest that the longitudinal instability in the flow down a slope is the long-wave instability of the kinematic wave in a quasi-one-dimensional system for all of regimes A, B, and C.

One may think that, in regime C, which lies in the region of non-monotonic density profile in the case of $\phi = 0.05$ (figure 6), the non-monotonic density profile might play a crucial role in the instability as in the case of the transverse instability of Rayleigh–Bérnard type, where the convection occurs due to the non-monotonic density profile (Forterre & Pouliquen 2002; Carpen & Brady 2002); however, the fact that regime C contains part of the region of monotonic density profile in the case of $\phi = 0.10$ (figure 12) suggests that the shape of the density profile does not determine the instability. It should also be noted that the present longitudinal instability occurs at long wavelength while the transverse instability appears at finite wavelength.

5.1.2. *One-dimensional model*

In order to confirm that the longitudinal instability is the long-wave instability of the one-dimensional kinematic wave, we now try to reduce our two-dimensional model into a one-dimensional model that preserves the major features of the original model. In spite of the crudeness of our procedure, we will see the one-dimensional model obtained has roughly the same stability diagram for the long-wave instability of the kinematic wave.

We obtain the one-dimensional model by integrating the original equations in the y-direction from 0 to ∞; the idea is similar to Valance & Pennec (1998), where the one-dimensional model has been obtained for the flow in a vertical chute by integrating the equations across the chute width.

We define the one-dimensional density $\bar{\rho}(x, t)$, the average velocity $\bar{u}(x, t)$, and the average temperature $\bar{T}(x, t)$ as

$$\bar{\rho}(x, t) \equiv \int_0^\infty \nu(x, y, t)\, \mathrm{d}y, \tag{5.3}$$

$$\bar{\rho}(x, t)\bar{u}(x, t) \equiv \int_0^\infty \nu(x, y, t) u(x, y, t)\, \mathrm{d}y, \tag{5.4}$$

$$\bar{\rho}(x, t)\bar{T}(x, t) \equiv \int_0^\infty \nu(x, y, t) T(x, y, t)\, \mathrm{d}y. \tag{5.5}$$

The one-dimensional equation of continuity obtained by integrating (2.1) is

$$\partial_t \bar{\rho} + \partial_x(\bar{\rho}\bar{u}) = 0, \tag{5.6}$$

where ∂_t and ∂_x represent $\partial/\partial t$ and $\partial/\partial x$, respectively. Equation (5.6) is in the form of (5.1) with the flux $Q(x, t)$ given by $Q = \bar{\rho}\bar{u}$.

By integrating the x-component of the equation of motion (2.2), we obtain

$$\partial_t(\bar{\rho}\bar{u}) + \partial_x \int_0^\infty \nu(x, y, t) u(x, y, t)^2\, \mathrm{d}y = \bar{\rho} \sin\theta + \Sigma_{yx}(\nu(0), T(0), u(0)) - \partial_x \left(\int_0^\infty \Sigma_{xx}(\nu, T, u)\, \mathrm{d}y \right), \tag{5.7}$$

which determines the evolution of $Q = \bar{\rho}\bar{u}$. The second term on the right-hand side is the shear stress at the floor and comes from the integration of $\partial_y \Sigma_{yx}$.

To simplify (5.7), we make the following approximations: (i) Replace the second term on the left-hand side by $\bar{\rho}\bar{u}^2$. (ii) Neglect the velocity in the y-direction, v, and use the dilute-limit expressions for the pressure and viscosities in Σ_{xx}, namely replace Σ_{xx} by $\nu T - (4/3) f_2(0)\sqrt{T}\partial_x u$, where the first term comes from the pressure and the second term comes from the dilute limit of the shear viscosity. The second viscosity $\zeta(\nu, T)$ is neglected because it is a higher-order quantity in ν (see (2.7)).

(iii) Estimate the integration of the shear viscosity term by multiplying the integrand by the decay length of the density ($T/\cos\theta$), and replacing T by $\bar{T}$, u by $\bar{u}$, i.e. replace $(4/3)f_2(0)\int_0^\infty(\sqrt{T}\partial_x u)\,\mathrm{d}y$ by $H(\bar{T})(4/3)f_2(0)(\sqrt{\bar{T}}\partial_x\bar{u})$, where $H(\bar{T})=\bar{T}/\cos\theta$.

Then we obtain the equation

$$\partial_t(\bar{\rho}\bar{u})+\partial_x(\bar{\rho}\bar{u}^2)=\bar{\rho}\sin\theta+\Sigma_{yx}(\nu(0),T(0),u(0))-\partial_x(\bar{\rho}\bar{T})+(4/3)f_2(0)\partial_x(H(\bar{T})\sqrt{\bar{T}}\partial_x\bar{u}). \tag{5.8}$$

For the shear stress at the floor $\Sigma_{yx}(\nu(0),T(0),u(0))$, we have the boundary condition of momentum balance (2.9), i.e. $\Sigma_{yx}(\nu(0),T(0),u(0))=-\eta^*(\nu(0),T(0))u(0)$.

To close equations (5.6) and (5.8), we need the relation between $(\nu(0),T(0),u(0))$ and $(\bar{\rho},\bar{T},\bar{u})$, and the equation for the average temperature $\bar{T}$. We simply assume that $u(0)=\bar{u}$ and $T(0)=\bar{T}$, and we use the empirical relation between $\nu(0)$ and $\bar{\rho}$ for steady flows; namely, we take $\nu(0)=F(\bar{\rho})$, with the form of $F(\bar{\rho})$ determined from the steady solution obtained numerically for a fixed θ and different values of $\nu_0(0)$ by using $\nu_0(0)=F(\bar{\rho}_0)$ with $\bar{\rho}_0=\int_0^\infty\nu_0(y)\,\mathrm{d}y$. We further assume that $\bar{T}$ is also determined by the one-dimensional density $\bar{\rho}$, rather than using the integrated equation for the temperature. The form of $\bar{T}=\bar{T}(\bar{\rho})$ is determined from the steady flows, namely we assume $\bar{T}_0=(1/\bar{\rho}_0)\int_0^\infty\nu_0(y)T_0(y)\,\mathrm{d}y=\bar{T}(\bar{\rho}_0)$.

Now we finally obtain the one-dimensional model in the following form:

$$\partial_t\bar{\rho}+\partial_x(\bar{\rho}\bar{u})=0, \tag{5.9}$$

$$\bar{\rho}[\partial_t\bar{u}+\bar{u}\partial_x\bar{u}]=a(\bar{\rho})[U(\bar{\rho})-\bar{u}]-\partial_x(\bar{\rho}\bar{T}(\bar{\rho}))+\tfrac{4}{3}f_2(0)\partial_x\left(H(\bar{T}(\bar{\rho}))\sqrt{\bar{T}(\bar{\rho})}\partial_x\bar{u}\right), \tag{5.10}$$

where

$$a(\bar{\rho})=\eta^*(F(\bar{\rho}),\bar{T}(\bar{\rho})),\quad U(\bar{\rho})=\frac{\bar{\rho}\sin\theta}{a(\bar{\rho})}. \tag{5.11}$$

In this model, the steady solution is given by $\bar{\rho}=\rho_0=\text{const.}$ and $\bar{u}=U(\rho_0)$, and the flux of the steady solution is given by $q_0=\rho_0U(\rho_0)$. Equation (5.10) with (5.11) shows that the velocity $U(\rho_0)$ is determined by the balance between the acceleration due to the gravity and the drag force from the floor.

This model is almost the same form as the traffic flow model proposed by Kerner & Konhäuser (1993), but with a different form of the function $U(\bar{\rho})$. In the traffic flow model, $U(\bar{\rho})$ is often called the 'optimal velocity function', which defines the density dependence of the car velocity and is usually a decreasing function. On the other hand, in the case of granular flow on a slope, $U(\bar{\rho})$ depends on the inclination angle and the boundary condition at the floor, and can take various forms as can be seen in the plot of $\bar{\rho}_0$ vs. $Q_0\approx q_0=\bar{\rho}_0U(\bar{\rho}_0)$† in figures 2(*b*) and 4(*b*).

A linear stability analysis of the steady solution can be performed analytically (for the traffic flow model, see e.g. Wada & Hayakawa 1998). It is easy to show that the instability condition $\mathrm{Re}(\alpha)>0$ yields

$$(a(\rho_0)U'(\rho_0))^2k^2>\left(\frac{a(\rho_0)}{\rho_0}+\bar{\mu}(\rho_0)k^2\right)^2(\rho_0\bar{T}(\rho_0))'k^2, \tag{5.12}$$

† The flux q_0 in the one-dimensional model is not exactly the same as the flux Q_0 in the original two-dimensional flow, due to the approximations used to derive $U(\bar{\rho})$.

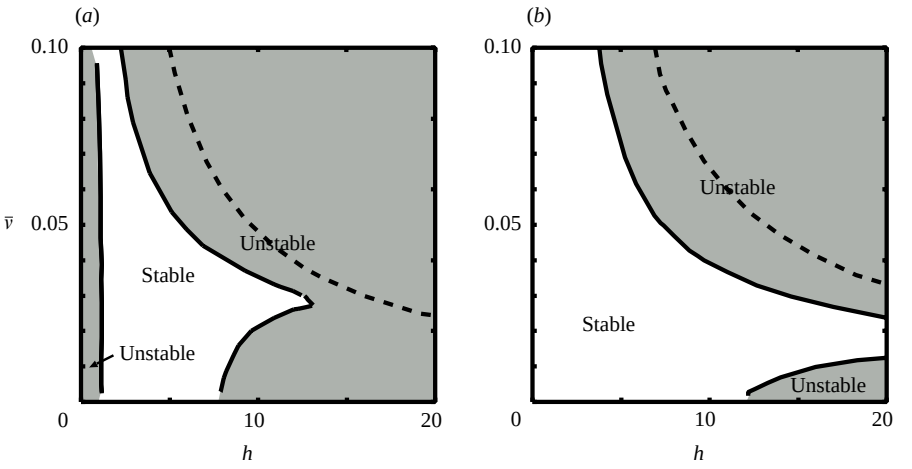

FIGURE 15. The stability diagram for (*a*) $\phi = 0.05$ and (*b*) $\phi = 0.10$ obtained from the one-dimensional model. The unstable (stable) regimes are shown in grey (white). The dashed line shows the boundary between the region of non-monotonic density profiles and that of monotonic density profiles for the original model.

where $\bar{\mu}(\rho_0) \equiv (4/3) f_2(0) H(\bar{T}(\rho_0)) \sqrt{\bar{T}(\rho_0)}$ and the prime represents differentiation by ρ_0. The $k \to 0$ limit of (5.12) gives the stability criterion,

$$(\rho_0 U'(\rho_0))^2 > (\rho_0 \bar{T}(\rho_0))'. \tag{5.13}$$

The explicit form of the long-wavelength expansion of the dispersion relation for the least stable mode is given by

$$\alpha(k) = -(\rho_0 U(\rho_0))' \mathrm{i}k + \frac{\rho_0}{a(\rho_0)} [(\rho_0 U'(\rho_0))^2 - (\rho_0 \bar{T}(\rho_0))'] k^2 + O(k^3), \tag{5.14}$$

and we see that the phase velocity of this mode in the long-wavelength limit is given by $c = -(\rho_0 U(\rho_0))' = -\mathrm{d}q_0/\mathrm{d}\rho_0$, which shows that this is a kinematic wave. The instability arises when the coefficient of the k^2 term becomes positive, which occurs if the change of the velocity with respect to density fluctuation is too fast compared to the effect of the pressure which reduces the density fluctuation. Note that the criterion of the instability (5.13) does not depend on the shear viscosity term $\bar{\mu}(\rho_0)$ because it only appears in the fourth-order term in k (see (5.12)); the approximation for that term does not crucially affect on the criterion.

The stability diagrams for $\phi = 0.05$ and $\phi = 0.10$ obtained from this one-dimensional model are shown in figure 15. In spite of the crude approximations used in the derivation of the one-dimensional model, the stability diagrams are qualitatively similar to those of the original model. The similarity further indicates that density wave formation can be understood by the long-wave instability in quasi-one-dimensional systems, as in film flow and traffic flow.

It should be noticed that, in this one-dimensional model, the effect of the parameters in the original model, such as e_p, ϕ, and Φ, is included more or less implicitly in the functional forms of $U(\bar{\rho})$ and $\bar{T}(\bar{\rho})$ (ϕ also appears explicitly in (5.11) through η^*), and the y-dependences of the variables also affect $U(\bar{\rho})$ and $\bar{T}(\bar{\rho})$ through the integration. Any changes that affect U and $\bar{T}$ result in changes of the unstable regions (see criterion (5.13)), although the nature of the instability remains the same.

Before concluding this subsection, let us make a few comments on the work by Wang, Jackson & Sundaresan (1997) and Valance & Pennec (1998) on the stability analysis of granular flow in a vertical chute using hydrodynamic models of rapid granular flow; Wang *et al.* (1997) performed the linear stability analysis numerically as in the present work, and Valance & Pennec (1998) analysed the density wave by deriving a one-dimensional model from hydrodynamic equations for rapid flow.

In the analysis of Wang *et al.* (1997), a parameter region has been found where the steady flow is unstable to a longitudinal long-wavelength perturbation and forms a density wave (figures 9 and 10 in Wang *et al.* 1997). This instability might also be understood as the long-wave instability observed in the present analysis. On the other hand, they also found the instabilities for finite-wavelength perturbations, which has not been observed here.

The analysis by Valance & Pennec (1998) shows a clear similarity between the instability in the chute flow and in the slope flow. The one-dimensional model they obtained has a mathematical structure and physical mechanism similar to those of our one-dimensional model: the velocity of the steady solution is determined by the balance of the gravitational acceleration and the drag force from the wall, and shows the long-wave instability for which the criterion is determined by the change of the velocity with respect to density fluctuations and the pressure term.

These results suggest that the instabilities in the vertical chute flow and the slope flow are of the same class.

5.2. *Comparison with molecular dynamics simulations*

We find some qualitative agreements between the present results and our previous simulations (Mitarai & Nakanishi 2001) as follows.

Our simulations were performed for a fixed inclination angle and a particular roughness of the slope with the periodic boundary condition imposed along the flow direction. Within the parameter region examined, the steady flow shows a monotonic density profile (Mitarai *et al.* 2002), and the flow with lower density has higher velocity.

It has been demonstrated that the density wave appears only in a long system with low enough particle density. We have performed the simulations for several sets of the slope length L and the particle number N. In the case of particle density $N\sigma/L \approx 1.0$ (single layer), a clear density wave is not formed for $L = 250.5\sigma$ and $L = 501\sigma$, whereas a density wave appears for $L = 1002\sigma$. Upon changing the density with a fixed system length $L = 501\sigma$, a density wave is formed when $N\sigma/L \approx 0.75$, while the steady flow is stable for the denser cases with $N\sigma/L \approx 1.0$ and 2.0.

These trends of the simulations agree with the behaviour around the unstable regime B of the present model on three points: (i) the flow with lower density is faster; (ii) the flow with lower density is less stable; and (iii) the critical wavelength for instability is very long.

Regarding (iii), the critical wavelength $\lambda_c = 2\pi/k_c$ is much longer than the particle diameter: $\lambda_c \approx 900\sigma$ for $\theta = 16^\circ$ and $\nu_0(0) = 0.05$, for example. This seems to be comparable with our simulation results, where the critical slope length L_c was between 500σ and 1000σ for $N\sigma/L \approx 1.0$. We do not understand yet how such a small wavenumber arises, but we suspect that it comes from the long mean free path in the large-y region where the density is low, namely the particles flying over the clusters for a long distance prevent the growth of clusters at a smaller length scale.

Based on observations (i), (ii), and (iii), the parameters that we have simulated happen to be in regime B, but if the simulations are performed with different

densities, inclination angles, and/or boundary conditions at the floor, behaviour that corresponds to regime A or C may be found.

5.3. *Comparison with the stability analysis for the transverse perturbations*

Forterre & Pouliquen (2002) examined the linear stability of granular flow on a wide slope to perturbations transverse to the flow direction, in order to understand the regular streak pattern along the flow direction observed in their experiments (Forterre & Pouliqen 2001). They mainly focused on the parameter region where the non-monotonic density profile (or what they call the 'inverted density profile') is observed, because they expected that such a flow would be unstable and form the vortex rolls from the analogy to the Rayleigh–Bérnard instability. They have shown that the flow is unstable to transverse perturbations in a large part of the parameter region where the inverted density profile is observed. The unstable mode shows the vortex-like pattern, and they concluded that the streaks observed in the experiments result from the rolls of vortices. They also found that the flow with a monotonic density profile becomes unstable for some parameters, but the details were not reported.

One of the differences between this transverse Rayleigh–Bérnard-type instability and the longitudinal long-wave instability appears in the length scale of the instability. The longitudinal instability occurs for long-wavelength perturbations in the long-time behaviour as can be seen in the dispersion relations, while the transverse instability occurs at a finite length scale comparable with the vortex roll. Our analysis shows that there is a parameter region where both of the instabilities may occur, around the region of non-monotonic density profiles (regime C). It should be interesting to investigate whether the two instabilities interfere by a full three-dimensional analysis.

At large inclination angle, Forterre & Pouliquen (2002) also observed the square lattice pattern. This phenomenon cannot be understood by the simple superposition of the long-wave instability and the Rayleigh–Bérnard-type instability, because the length scale of the long-wave instability is much longer than that of the lattice pattern.

6. Summary

Steady flows and their linear stability are analysed for granular flow on a slope using the hydrodynamic model with constitutive relations derived from the kinetic theory of inelastic spheres. We have mainly focused on the relatively low-density region where the density decays monotonically.

The stability diagram shows three unstable regimes A, B, and C for both $\phi = 0.05$ and $\phi = 0.10$. Two of the unstable regimes, A and B, are in the lower density region, and regime C is in the high-density region. The difference between regimes A and B is that the denser flow is faster in regime A on the small-h side, while the flow with lower density is faster in regime B on the large-h side. Regime C is in the large-h and large $\bar{\nu}$-region; it lies within the region of non-monotonic density profile for $\phi = 0.05$, while it contains part of the region of monotonic density profiles for $\phi = 0.10$, although the region of regime C roughly corresponds to that of non-monotonic density profile. In all regimes, the instability occurs for the long-wavelength perturbations and results in the formation of a density wave. It has been found that the behaviour around the unstable regime B agrees with the trends in our previous simulations of density wave formation.

The dispersion of the complex growth rate $\alpha(k)$ has the features that (i) $\alpha(0) = 0$, (ii) $\mathrm{Re}(\alpha(k)) \propto k^2$ for small k, and (iii) $\mathrm{Im}(\alpha(k))/k = -\mathrm{d}Q_0/\mathrm{d}\bar{\rho}_0$ in the

long-wavelength limit. These strongly suggest that the instability is the long-wave instability of kinematic waves, which is often found in quasi-one-dimensional flows. This is different from the transverse instability studied by Forterre & Pouliquen (2002), where the flow is unstable at finite wavenumber.

In order to confirm that the instability is the long-wave instability of a kinematic wave, we simplified the original equations rather heuristically to a one-dimensional model, and showed that the long-wave instability occurs in the derived one-dimensional model. The stability diagram obtained from the one-dimensional model corresponds qualitatively to the one obtained from the original equations.

N. M. is grateful to Ooshida Takeshi for informative discussions. This work was partially supported by Hosokawa powder technology foundation and Grant-in-Aid for JSPS fellows.

Appendix A. Linearized equations

The linearized governing equations for the longitudinal perturbations (4.1)–(4.3) and the boundary conditions are given (Forterre & Pouliquen 2002, see also Alam & Nott 1998). The superscript 0 denotes that the quantities are for the steady solution. The subscripts ν and T denote partial derivatives with respect to the variables

$$p^0_\nu = \partial p(\nu, T)/\partial \nu|_{\nu=\nu_0, T=T_0}.$$

The subscript y indicates the total differential with respect to y, namely

$$\begin{aligned} p^0_y &= \mathrm{d}p^0(\nu(y), T(y))/\mathrm{d}y \\ &= \left[\partial p(\nu, T)/\partial \nu|_{\nu=\nu_0, T=T_0}\right]\nu_{0,y} + \left[\partial p(\nu, T)/\partial T|_{\nu=\nu_0, T=T_0}\right]T_{0,y},\ \nu_{0,y} = \mathrm{d}\nu_0(y)/\mathrm{d}y, \end{aligned}$$

and so on. The expressions for $p(\nu, T)$, $\mu(\nu, T)$, $\zeta(\nu, T)$, $\kappa(\nu, T)$, and $\Gamma(\nu, T)$ are given in (2.7), and $\xi(\nu, T) = \zeta - 2\mu/3$. Then, by inserting (4.1)–(4.3) into (2.1)–(2.3) to (3.1)–(3.3), we obtain the following expressions:

$$[\partial_t + u_0\partial_x]\nu_1 + [\nu_0\partial_x]u_1 + [\nu_{0,y} + \nu_0\partial_y]v_1 = 0, \tag{A 1}$$

$$\begin{aligned} &\left[\sin\theta - p^0_\nu\partial_x + u_{0,yy}\mu^0_\nu + u_{0,y}\mu^0_{\nu,y} + u_{0,y}\mu^0_\nu\partial_y\right]\nu_1 \\ &\quad + \left[-\nu_0\partial_t - \nu_0 u_0\partial_x + (\xi^0 + 2\mu^0)\partial_x^2 + \mu^0_y\partial_y + \mu^0\partial_y^2\right]u_1 \\ &\quad + \left[-\nu_0 u_{0,y} + \mu^0_y\partial_x + (\xi^0 + \mu_0)\partial_x\partial_y\right]v_1 \\ &\quad + \left[-p^0_T\partial_x + u_{0,yy}\mu^0_T + u_{0,y}\mu^0_{Ty} + u_{0,y}\mu^0_T\partial_y\right]T_1 = 0, \end{aligned} \tag{A 2}$$

$$\begin{aligned} &\left[-\cos\theta - p^0_{\nu y} - p^0_\nu\partial_y + u_{0,y}\mu^0_\nu\partial_x\right]\nu_1 \\ &\quad + \left[\xi^0_y\partial_x + \xi^0\partial_x\partial_y + \mu^0\partial_x\partial_y\right]u_1 \\ &\quad + \left[-\nu_0\partial_t - \nu_0 u_0\partial_x + \xi^0_y\partial_y + \xi^0\partial_y^2 + 2\mu^0_y\partial_y + 2\mu_0\partial_y^2 + \mu_0\partial_x^2\right]v_1 \\ &\quad + \left[-p^0_{Ty} - p^0_T\partial_y + u_{0,y}\mu^0_T\partial_x\right]T_1 = 0, \end{aligned} \tag{A 3}$$

$$\begin{aligned} &\left[\kappa^0_{\nu y}T_{0,y} + \kappa^0_\nu T_{0,yy} + \kappa^0_\nu T_{0,y}\partial_y - \Gamma^0_\nu + u^2_{0,y}\mu^0_\nu\right]\nu_1 \\ &\quad + \left[-p^0\partial_x + 2\mu^0 u_{0,y}\partial_y\right]u_1 \\ &\quad + \left[-\tfrac{3}{2}\nu_0 T_{0,y} - p^0\partial_y + 2\mu^0 u_{0,y}\partial_x\right]v_1 \\ &\quad + \left[-\tfrac{3}{2}\nu_0\partial_t - \tfrac{3}{2}\nu_0 u_0\partial_x + \kappa^0\partial_x^2 + \kappa^0_y\partial_y + \kappa^0\partial_y^2\right. \\ &\quad \left. + \kappa^0_{Ty}T_{0,y} + \kappa^0_T T_{0,yy} + \kappa^0_T T_{0,y}\partial_y - \Gamma^0_T + u^2_{0,y}\mu^0_T\right]T_1 = 0. \end{aligned} \tag{A 4}$$

The linearized boundary conditions at $y = 0$ are obtained from (2.9) and (2.10) as

$$\partial_y u_1 = \phi\left[u_0 f^0_{7,\nu}\nu_1 + f^0_7 u_1\right], \tag{A 5}$$

$$\partial_y T_1 = -f^0_{6,\nu}\left[\tfrac{1}{3}\phi u_0^2 - \tfrac{1}{2}\Phi T_0\right]\nu_1 - f^0_6\left[\tfrac{2}{3}\phi u_0 u_1 - \tfrac{1}{2}\Phi T_1\right]. \tag{A 6}$$

Appendix B. The long-wavelength limit of the phase velocity

We have obtained the dispersion relation of the least stable mode, $\alpha = \alpha(k)$, and numerically found that it satisfies

$$\alpha(0) = 0. \tag{B 1}$$

In this appendix, we show that the phase velocity of this mode, $c = \mathrm{Im}(\alpha(k))/k$, satisfies

$$c = -\frac{\mathrm{d}Q_0}{\mathrm{d}\bar{\rho}_0} \tag{B 2}$$

in the long-wavelength limit ($k \to 0$), which suggests the mode is a kinematic wave. Here, $\bar{\rho}_0$ and Q_0 are the one-dimensional density and the flux of the steady solution, respectively, defined in (3.15).

Note that the derivative $\mathrm{d}Q_0/\mathrm{d}\bar{\rho}_0$ is taken within a family of solutions for a fixed inclination angle as below. For a given inclination angle, the density at the floor $\nu_0(0) = \beta$ is a continuous parameter to specify a steady solution. To express the β dependence explicitly, we rewrite the steady solutions as

$$\nu(x, y, z, t) = \nu_0(y;\beta), \tag{B 3}$$

$$\boldsymbol{u}(x, y, z, t) = (u_0(y;\beta), 0, 0), \tag{B 4}$$

$$T(x, y, z, t) = T_0(y;\beta). \tag{B 5}$$

Then $\mathrm{d}Q_0/\mathrm{d}\bar{\rho}_0$ is given by

$$\frac{\mathrm{d}Q_0}{\mathrm{d}\bar{\rho}_0} = \frac{\mathrm{d}Q_0(\beta)/\mathrm{d}\beta}{\mathrm{d}\bar{\rho}_0(\beta)/\mathrm{d}\beta} = \frac{\displaystyle\int_0^\infty [\partial(\nu_0(y;\beta)u_0(y;\beta))/\partial\beta]\,\mathrm{d}y}{\displaystyle\int_0^\infty [\partial\nu_0(y;\beta)/\partial\beta]\,\mathrm{d}y}. \tag{B 6}$$

In order to verify (B 2), let us first express c by eigenfunctions of the mode. By linearization of the equation of continuity (2.1) using (4.4), we obtain the following expression:

$$\alpha\hat{\nu}(y) = -\mathrm{i}k\,(\nu_0(y;\beta)\hat{u}(y) + u_0(y;\beta)\hat{\nu}(y)) - \partial_y(\nu_0(y;\beta)\hat{v}(y)). \tag{B 7}$$

Integrating (B 7) from $y = 0$ to ∞, we have

$$\alpha\int_0^\infty \hat{\nu}(y)\mathrm{d}y = -\mathrm{i}k\int_0^\infty [\nu_0(y;\beta)\hat{u}(y) + u_0(y;\beta)\hat{\nu}(y)]\,\mathrm{d}y. \tag{B 8}$$

Here, $\hat{\nu}(y)$, $\hat{u}(y)$, $\hat{v}(y)$, and $\hat{T}(y)$ depend on the wavenumber k, and we expand these functions with respect to k, i.e.

$$\hat{\nu}(y) = \hat{\nu}_0(y) + \mathrm{i}k\hat{\nu}_1(y) + \cdots, \qquad \hat{u}(y) = \hat{u}_0(y) + \mathrm{i}k\hat{u}_1(y) + \cdots, \tag{B 9}$$

$$\hat{v}(y) = \hat{v}_0(y) + \mathrm{i}k\hat{v}_1(y) + \cdots, \qquad \hat{T}(y) = \hat{T}_0(y) + \mathrm{i}k\hat{T}_1(y) + \cdots, \tag{B 10}$$

where $(\hat{\nu}_i(y), \hat{u}_i(y), \hat{v}_i(y), \hat{T}_i(y))$ do not contain k. The long-wavelength expansion of the dispersion relation $\alpha = \alpha(k)$ which satisfies $\alpha(0) = 0$ is obtained from (B 8) when

$\int_0^\infty \hat{v}_0(y)\,\mathrm{d}y \neq 0$, and we have

$$\alpha(k) = -\mathrm{i}k\frac{\displaystyle\int_0^\infty [\nu_0(y;\beta)\hat{u}_0(y) + u_0(y;\beta)\hat{v}_0(y)]\,\mathrm{d}y}{\displaystyle\int_0^\infty \hat{v}_0(y)\,\mathrm{d}y} + O(k^2). \tag{B 11}$$

Namely, c is given by

$$c = -\frac{\displaystyle\int_0^\infty [\nu_0(y;\beta)\hat{u}_0(y) + u_0(y;\beta)\hat{v}_0(y)]\,\mathrm{d}y}{\displaystyle\int_0^\infty \hat{v}_0(y)\,\mathrm{d}y} \tag{B 12}$$

in the long-wavelength limit.

Now all we need to do is to express $\hat{\boldsymbol{X}}_0 \equiv (\hat{\nu}_0, \hat{u}_0, \hat{v}_0, \hat{T}_0)$ with respect to the steady solution $\boldsymbol{X}_0(y;\beta) \equiv (\nu_0(y;\beta), u_0(y;\beta), 0, T_0(y;\beta))$. Let us write (2.1)–(2.3) and the boundary conditions in the matrix form:

$$\boldsymbol{B}\frac{\partial \boldsymbol{X}}{\partial t} = \boldsymbol{N}(\boldsymbol{X}). \tag{B 13}$$

Here, $\boldsymbol{X} = (\nu, u, v, T)$, $\boldsymbol{B}$ is a constant matrix, and $\boldsymbol{N}$ is a nonlinear operator. A steady solution $\boldsymbol{X}_0(y;\beta)$ satisfies

$$\boldsymbol{N}(\boldsymbol{X}_0(y;\beta)) = 0; \tag{B 14}$$

therefore, from (4.4), $\hat{\boldsymbol{X}} = (\hat{\nu}, \hat{u}, \hat{v}, \hat{T})$ satisfies

$$\left.\frac{\partial \boldsymbol{N}(\boldsymbol{X}))}{\partial \boldsymbol{X}}\right|_{\boldsymbol{X}=\boldsymbol{X}_0(y;\beta)} \hat{\boldsymbol{X}} = \alpha(k) B \hat{\boldsymbol{X}}, \tag{B 15}$$

and expanding (B 15) in k with $\alpha(0) = 0$, we have

$$\left.\frac{\partial \boldsymbol{N}(\boldsymbol{X}))}{\partial \boldsymbol{X}}\right|_{\boldsymbol{X}=\boldsymbol{X}_0(y;\beta)} \hat{\boldsymbol{X}}_0 = 0 \tag{B 16}$$

for the lowest order of k. On the other hand, differentiating (B 14) by β, we obtain

$$\frac{\partial \boldsymbol{N}(\boldsymbol{X}))}{\partial \boldsymbol{X}}|_{\boldsymbol{X}=\boldsymbol{X}_0(y;\beta)} \frac{\partial \boldsymbol{X}_0(y;\beta)}{\partial \beta} = 0. \tag{B 17}$$

It is plausible that the mode of the zero eigenvalue for $k = 0$ does not degenerate, because the mass is the only conserved quantity (the momentum is lost at the floor, and the energy is dissipated). Thus, from (B 16) and (B 17), we obtain $\hat{\boldsymbol{X}}_0 \propto \partial \boldsymbol{X}_0(y;\beta)/\partial\beta$, or more explicitly,

$$(\hat{\nu}_0, \hat{u}_0, \hat{v}_0, \hat{T}_0) \propto \left(\frac{\partial \nu_0(y;\beta)}{\partial\beta}, \frac{\partial u_0(y;\beta)}{\partial\beta}, 0, \frac{\partial T_0(y;\beta)}{\partial\beta}\right). \tag{B 18}$$

Using (B 12) and (B 18), we obtain

$$c = -\frac{\displaystyle\int_0^\infty [\nu_0(y;\beta)(\partial u_0(y;\beta)/\partial\beta) + u_0(y;\beta)(\partial \nu_0(y;\beta)/\partial\beta)]\,\mathrm{d}y}{\displaystyle\int_0^\infty (\partial \nu_0(y;\beta)/\partial\beta)\,\mathrm{d}y}, \tag{B 19}$$

and by comparing this with (B 6), we have

$$c = -\frac{\mathrm{d}Q_0/\mathrm{d}\beta}{\mathrm{d}\bar{\rho}_0/\mathrm{d}\beta} = -\frac{\mathrm{d}Q_0}{\mathrm{d}\bar{\rho}_0}, \tag{B 20}$$

which is (B 2).

REFERENCES

Ahn, H., Brennen, C. E. & Sabersky, R. H. 1992 Analysis of the fully developed chute flow of granular materials. *Trans. ASME: J. Appl. Mech.* **59**, 109–119.

Alam, M. & Nott, P. R. 1998 Stability of plane Couette flow of a granular material. *J. Fluid Mech.* **377**, 99–136.

Anderson, E., Bai, Z., Bischof, C., Blackford, S., Demmel, J., Dongarra, J., Du Croz, J., Greenbaum, A., Hammarling, S., McKenney, A. & Sorensen, D. 1999 *LAPACK Users' Guide*, 3rd Edn. SIAM.

Anderson, K. G. & Jackson, R. 1992 A comparison of the solutions of some proposed equations of motion of granular materials for fully developed flow down inclined planes. *J. Fluid Mech.* **241**, 145–168.

Bando, M., Hasebe, K., Nakayama, A., Shibata, A. & Sugiyama, A. 1995 Dynamical model of traffic congestion and numerical simulation. *Phys. Rev.* E **51**, 1035–1042.

Boyd, J. P. 2001 *Chebyshev and Foulier Spectral Methods*, 2nd Edn. Dover.

Campbell, C. S. 1990 Rapid granular flows. *Annu. Rev. Fluid Mech.* **22**, 57–92.

Canuto, C., Hussaini, M. Y., Quarteroni, A. & Zang, T. A. 1988 *Spectral Methods in Fluid Dynamics*. Springer.

Carpen, I. C. & Brady, J. F. 2002 Gravitational instability in suspension flow. *J. Fluid Mech.* **472**, 201–210.

Cundall, P. A. & Strack, O. D. L. 1979 A discrete numerical model for granular assemblies. *Geotechnique* **29**, 47–65.

Forterre, Y. & Pouliquen, O. 2001 Longitudinal vortices in granular flows. *Phys. Rev. Lett.* **86**, 5886–5889.

Forterre, Y. & Pouliquen, O. 2002 Stability analysis of rapid granular chute flows: formation of longitudinal vortices. *J. Fluid Mech.* **467**, 361–387.

Goldhirsh, I. 2003 Rapid granular flows. *Annu. Rev. Fluid Mech.* **35** 267–293.

Gottlieb, D., Hussaini, M. Y. & Orszag, S. A. 1984 Theory and applications of spectral methods. In *Spectral Methods for Partial Differential Equations* (ed. R. G. Voigt, D. Gottlieb & M. Y. Hussaini). SIAM.

Jaeger, H. M., Nagel, S. R. & Behringer, R. P. 1996 Granular solids, liquids, and gases. *Rev. Mod. Phys.* **68**, 1259–1273.

Jenkins, J. T. 1992 Boundary conditions for rapid granular flow: flat, frictional walls. *J. Appl. Mech.* **59**, 120–127.

Jenkins, J. T. & Richman, M. W. 1986 Boundary conditions for plane flows of smooth, nearly elastic, circular disks. *J. Fluid Mech.* **171**, 53–69.

Jenkins, J. T. & Savage, S. B. 1983 A theory for the rapid flow of identical, smooth, nearly elastic, spherical particles. *J. Fluid Mech.* **130**, 187–202.

Johnson, P. C. & Jackson, R. 1987 Frictional-collisional constitutive relations for granular materials, with application to plane shearing. *J. Fluid Mech.* **176**, 67–93.

Johnson, P. C., Nott, P. & Jackson, R. 1990 Frictional-collisional equations of motion for particulate flows and their application to chutes. *J. Fluid Mech.* **210**, 501–535.

Kerner, B. S. & Konhäuser, P. 1993 Cluster effect in initially homogeneous traffic flow. *Phys. Rev.* E **48**, R2335–R2338.

Louge, M. Y. & Keast, S. C. 2001 On dense granular flows down flat frictional inclines. *Phys. Fluids* **13**, 1213–1233.

Lun, C. K. K. & Savage, S. B. 1986 The effects of an impact velocity dependent coefficient of restitution on stresses developed by sheared granular materials. *Acta Mech.* **63**, 15–44.

Lun, C. K. K., Savage, S. B., Jeffrey, D. J. & Chepurniy, N. 1984 Kinetic theories for granular flow: inelastic particles in Couette flow and slightly inelastic particles in a general flowfield. *J. Fluid Mech.* **223**, 223–256.

Malik, M. R. 1990 Numerical methods for hypersonic boundary layer stability. *J. Comput. Phys.* **86**, 376–413.

Mayer, E. W. & Powell, K. G. 1992 Viscous and inviscid instabilities of a trailing vortex. *J. Fluid Mech.* **245**, 91–114.

Mitarai, N., Hayakawa, H. & Nakanishi, H. 2002 Collisional granular flow as a micropolar fluid. *Phys. Rev. Lett.* **88**, 174301.

Mitarai, N. & Nakanishi, H. 2000*a* Convective instability and structure formation in traffic flow. *J. Phys. Soc. Japan* **69**, 3752–3761.

Mitarai, N. & Nakanishi, H. 2000*b* Spatiotemporal structure of traffic flow in a system with an open boundary. *Phys. Rev. Lett.* **85**, 1766–1769.

Mitarai, N. & Nakanishi, H. 2001 Instability of dilute granular flows on rough slope. *J. Phys. Soc. Japan* **70**, 2809–2812.

Mitarai, N. & Nakanishi, H. 2003 Hard-sphere limit of soft-sphere model for granular materials: Stiffness dependence of steady granular flow. *Phys. Rev.* E **67**, 021301.

Moriyama, O., Kuroiwa, N., Matsushita, M. & Hayakawa, H. 1998 4/3 law of granular particles flowing through a vertical pipe. *Phys. Rev. Lett.* **80**, 2833–2836.

Ooshida, T. 1999 Surface equation of falling film flows with moderate Reynolds number and large but finite Weber number. *Phys. Fluids* **11**, 3247–3269.

Pouliquen, O. 1999 Scaling laws in granular flows down rough inclined planes. *Phys. Fluids* **11**, 542–545.

Prasad, S. N., Pal, D. & Römkens, M. J. M. 2000 Wave formation on a shallow layer of flowing grains. *J. Fluid Mech.* **413**, 89–110.

Raafat, T., Hulin, J. P. & Herrmann, H. J. 1996 Density waves in dry granular media falling through a vertical pipe. *Phys. Rev.* E **53**, 4345–4350.

Richman, M. W. 1988 Boundary conditions based upon a modified Maxwellian velocity distribution for flows of identical, smooth, nearly elastic spheres. *Acta Mechanica* **75**, 227–240.

Savage, S. B. 1984 The mechanics of rapid granular flows. *Adv. Appl. Mech.* **24**, 289–366.

Smith, M. K. 1993 The mechanism for the long-wave instability in thin liquid films. *J. Fluid Mech.* **217**, 469–485.

Valance, A. & Pennec, T. L. 1998 Nonlinear dynamics of density waves in granular flows through narrow vertical channels. *Eur. Phys. J.* B **5**, 223–229.

Wang, C., Jackson, R. & Sundaresan, S. 1997 Instabilities of fully developed rapid flow of a granular material in a channel. *J. Fluid Mech.* **342**, 179–197.

Wada, S. & Hayakawa, H. 1998 Kink solution in a fluid model of traffic flow. *J. Phys. Soc. Japan* **67**, 763–766.

Whitham, G.B. 1974 *Linear and nonlinear waves*. John Wiley & Sons.